Oil & Gas Science and Technology – Rev. IFP Energies nouvelles **75**, 28 (2020)

https://doi.org/10.2516/ogst/2020019

Available online at:
ogst.ifpenergiesnouvelles.fr

Subsurface Fluid Injection and Energy Storage
Q. Li, M. Kühn (Guest editors)

REGULAR ARTICLE OPEN ACCESS

Numerical simulation and feasibility assessment of acid gas injection in a carbonate formation of the Tarim Basin, China

Xiaoyan Zhang[1,2], Qi Li[1,2,*], Liange Zheng[3], Xiaying Li[1,2], and Liang Xu[1,2]

[1] State Key Laboratory of Geomechanics and Geotechnical Engineering, Institute of Rock and Soil Mechanics, Chinese Academy of Sciences, Wuhan 430071, China
[2] University of Chinese Academy of Sciences, Beijing 100049, China
[3] Energy Geoscience Division, Lawrence Berkeley National Laboratory, Berkeley, CA 94720, USA

Received: 27 June 2019 / Accepted: 23 March 2020

Abstract. An enormous amount of acid gas, containing carbon dioxide (CO_2) and hydrogen sulfide (H_2S), is generated in the exploitation of oil and gas reservoirs in the Tarim Basin, China. An appropriate management plan is required to safely dispose of the acid gas, and common strategy considered for the safe disposal of acid gas is the injection of it into deep formations – this strategy mitigates greenhouse gas emissions and avoids costs associated with desulfurization. A feasibility assessment of acid gas injection requires a detailed investigation of the potential physical and geochemical impacts. Reactive transport simulations based on the mineralogical composition and the hydrochemical characteristics of a carbonate formation in the Tarim Basin were conducted to identify the physical and geochemical interactions of acid gas with the mineral matrix and formation water. Acid gas (59% CO_2 and 41% H_2S) was injected at a constant rate of 19 200 Nm^3/d for 25 years, and the simulation was run by the TMVR_EOSG module of the TOUGHREACT code for a period of 10 000 years. The results indicate that the minimum liquid saturation is much larger than the residual water saturation, and the pressure buildup is below the allowable pressure increase. Additionally, the porosity change is found to be negligible due to the small changes in calcite and quartz in the volume fraction. From this perspective, acid gas injection in the carbonate formation of the Tarim Basin seems feasible. Furthermore, the fast breakthrough of CO_2 can provide an advanced warning of a potential breakthrough of acid gas. Last, the injection rate can be increased to accelerate acid gas trapping, and the results could be used as guidance for future acid gas injection operations.

1 Introduction

With the increasing exploitation of sour hydrocarbon reservoirs, a growing volume of acid gas, consisting primarily of carbon dioxide (CO_2) and hydrogen sulfide (H_2S), is generated. The conventional sulfur recovery method, which converts sulfur compounds to elemental sulfur and directly emits residual CO_2 into the atmosphere, can be adopted to dispose of acid gas. However, the recovered sulfur is below the commodity standard, making it difficult to sell and increasing the accumulation of hazardous waste. Furthermore, residual CO_2 emissions aggravate global warming. Consequently, Acid Gas Injection (AGI) into depleted oil and gas reservoirs is gaining increasing attention as an alternative to mitigate greenhouse gas emissions and to avoid the costs of desulfurization. Actually, acid gas injection operations have been approved worldwide (British Columbia Geological Survey, 2003; Carroll *et al.*, 2009; Khan *et al.*, 2013; Li *et al.*, 2017; Miwa *et al.*, 2002), and feasibility of AGI operations in China has been analyzed (Li *et al.*, 2013; Liu *et al.*, 2012). However, the implementation of acid gas injection requires a proper assessment of the effects induced by the presence of acid gas.

During acid gas injection, CO_2 and H_2S both displace and dissolve in the formation waters. Afterwards, the dissolved CO_2 and H_2S undergo hydrolysis reactions leading to the generation of weakly acidic solutions. Subsequently, acidic brine leads to the dissolution of the host rock minerals. Dissolved ions and minerals may also further react to precipitate carbonates and other secondary minerals (De Silva *et al.*, 2015; Jia *et al.*, 2016; Talman, 2015; Zhu *et al.*, 2013). As a result, more exploration is needed in the pre-feasibility investigation phase on the potential impacts (including physical and geochemical properties) and the trapping evolution of acid gas (Bachu and Gunter, 2004; Cantucci *et al.*, 2015; De Silva *et al.*, 2015; Talman, 2015; Zhu *et al.*, 2013).

Many investigations investigated the geochemical effects of acid gas injection. Knauss *et al.* (2005) evaluated

* Corresponding author: qli@whrsm.ac.cn

the impacts of dissolved CO_2, as well as a mixture of dissolved CO_2 and H_2S, on a geological formation. In addition, Xiao *et al.* (2009) and Xu *et al.* (2007) developed models to estimate the gas-fluid-rock interactions, in which CO_2 was injected as a gas phase and H_2S was injected as an aqueous solute. As an analogue for CO_2 geological storage, the results suggest that the injection of additional H_2S is very similar to the injection of pure CO_2 (Knauss *et al.*, 2005; Xiao *et al.*, 2009; Xu *et al.*, 2007). However, the presence of iron-bearing minerals leads to the precipitation of pyrite, which influences mineral trapping. Schaef *et al.* (2010) reported results from laboratory tests of various basalts reacted with water equilibrated with supercritical CO_2 containing 1% H_2S for 181 days. The results showed that very rapid precipitation of pyrite appeared to inhibit carbonate mineralization reactions. Schaef *et al.* (2013) continued the work of Schaef *et al.* (2010) by extending the duration of experiments up to 3.5 years. They found that permanent carbonate mineralization was not impaired by pyrite formation reactions, though pyrite appeared to coat the surface and halt carbonate formation in previous shorter duration tests.

The investigations mentioned above have provided significant insight into the geochemical effects of acid gas injection. However, the partitioning phenomena occurring after acid gas injection are neglected. Bachu and Bennion (2009) first carried out a series of laboratory experiments to examine the chromatographic partitioning of acid gas injected into deep saline aquifers. The experiments were conducted with H_2S as an impurity in the CO_2 stream, at 2%, 5% and 30% concentrations under static and dynamic conditions. They found that there is a time lag between CO_2 and H_2S appearing in the effluent gas. In addition, the higher the fraction of H_2S in the injection stream is, the smaller the time lag between the CO_2 and H_2S breakthroughs. Then, Bachu *et al.* (2009) carried out numerical studies to replicate the laboratory results, including the breakthrough of CO_2 appearing ahead of H_2S.

Many other studies have been undertaken to investigate both the physical and geochemical effects of acid gas injection. Zheng *et al.* (2010) and (2013) simulated the coinjection of H_2S with CO_2 into a deep saline aquifer to study the leakage of supercritical CO_2 and H_2S mixtures along a preferential pathway to an overlying fresh-water aquifer and to study reactions of the gas mixture with that aquifer. They concluded that there is some delay observed between the arrival times of CO_2 and H_2S into the shallow aquifer. Nevertheless, the effect does not continue very long in duration, and H_2S comigrating with CO_2 is predicted to enter the aquifer once this stripping effect ceases. If there was a sufficient amount of ferrous iron supplied in the aquifer, the precipitation of pyrite could sequester a large portion of the injected sulfide. Similarly, Zhang *et al.* (2011) performed numerical simulations to study the coinjection of H_2S and CO_2 in sandstone and carbonate formations. The chromatographic partitioning of acid gas was also observed. Moreover, they found that the presence of iron-bearing siliciclastic and carbonate was more favorable to H_2S mineral trapping. As a result, coinjection of H_2S in the CO_2 stream decreased the solubility and mineral trapping of CO_2 compared to the pure CO_2 injection case. Conversely, Bacon *et al.* (2014) found that co-sequestering H_2S along with CO_2 did not noticeably modify the predicted amount of CO_2 sequestered. Under this condition, up to 5% of H_2S is sequestered completely as pyrite.

Although acid gas injection has been investigated extensively, those studies only consider the effects of an H_2S impurity in CO_2 storage, including the partitioning phenomena of impure CO_2 storage, geochemical effects by coinjected H_2S and CO_2 storage capacity influenced by H_2S. The H_2S concentration in the injected CO_2 stream is lower than 10%. However, the H_2S concentration in acid gas injection operations varies from 2% to 85% (British Columbia Geological Survey, 2003). Essentially, water in the porous media becomes saturated with more soluble gas more quickly. In addition, a higher fraction of H_2S in the acid gas results in an earlier breakthrough of both CO_2 and H_2S (Bachu and Bennion, 2009; Bachu *et al.*, 2009). Additionally, more site-specific studies considering the variability and uncertainty of key hydrogeological and geochemical parameters are needed (Zheng *et al.*, 2013). Thus, the feasibility of acid gas injection in the Tarim Basin is urgently needed that considers the effect of acid gas composition (59% CO_2 and 41% H_2S), mineral composition, formation water chemistry and reservoir physical conditions.

In the present study, a numerical simulation was conducted to investigate the feasibility assessment of acid gas injection in a carbonate formation of the Tarim Basin. Four aspects were mainly considered: (1) the distribution of the acid gas plume and partitioning phenomenon occurring between CO_2 and H_2S; (2) the pressure buildup due to acid gas injection; (3) the geochemical effects and corresponding effects on the porosity of the reservoir; and (4) the trapping evolution of injected acid gas, including the acid gas mixture, CO_2 component and H_2S component. Finally, we considered the uncertainty of key parameters, including the injection rate, permeability and porosity, and performed a sensitivity analysis to investigate their impact on the evolution of gas saturation, pressure buildup and entrapment of injected acid gas.

2 Geological setting

The Tarim Basin is the largest sedimentary basin in China, with an area of approximately 560 000 km^2. The formation and evolution of the basin can be divided into four main periods: Sinian-Cambrian, Ordovician, early Permian, and Cretaceous (Chen *et al.*, 1997). As the largest petroliferous superposed basin in China, it has been well studied geologically (Chen *et al.*, 1997; Gao *et al.*, 2016; Jia *et al.*, 2016; Shen *et al.*, 2016), however, its potential as a site for acid gas injection has not yet been investigated. In this section, the geological setting of the Tahe oilfield is briefly addressed in Section 2.1 and the selected injection reservoir is presented in Section 2.2.

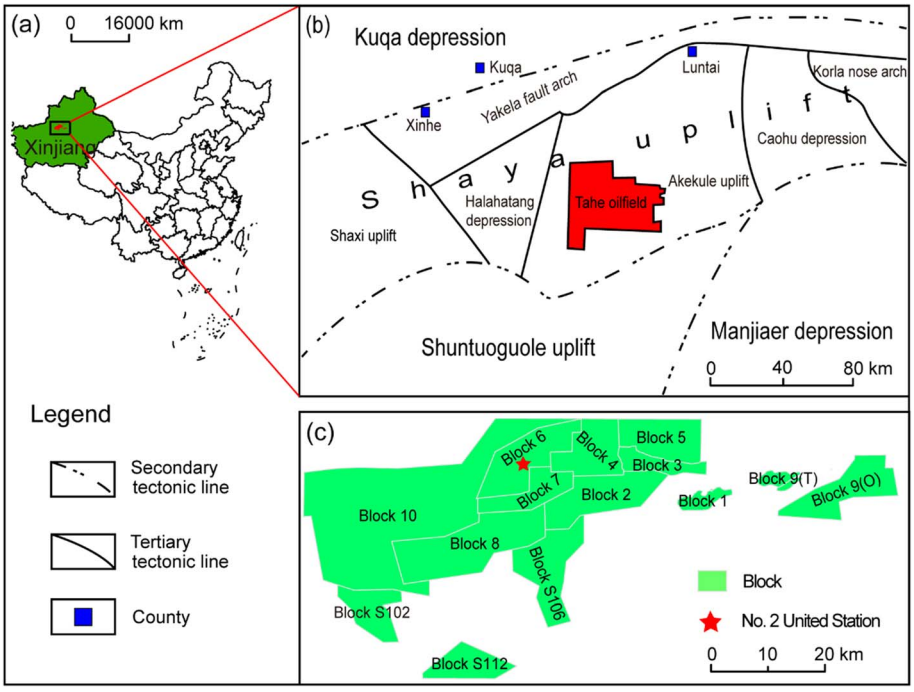

Fig. 1. Location map of the No. 2 United Station at the Tahe oilfield, Tarim Basin, Xinjiang, China.

2.1 Tahe oilfield

The Tahe oilfield, located in the northern Tarim Basin (Fig. 1a), is in the southwest Akekule uplift in the Shaya uplift. It is surrounded by the Caohu sag to the east, the Halahatang sag to the west, the Manjiaer sag to the south and the Yakela uplift to the north (Fig. 1b). The origin of petroleum in the Tahe oilfield is mainly Cambrian-Ordovician source rocks. To date, the Tahe oilfield, with its 12 blocks (Fig. 1c), is the largest oilfield found in the Paleozoic marine carbonate rocks in China. Petroleum is recovered from the Ordovician carbonate rocks and the Carboniferous and Triassic sandstones (Yu *et al.*, 2011).

2.2 Carbonate reservoir

The No. 2 United Station is located in Block 6 of the Tahe oilfield (Fig. 1c). It generates a large amount of acid gas as a byproduct during crude oil processing. To reduce greenhouse gas emissions and reduce the costs of desulfurization, the *SINOPEC* intends to dispose of acid gas in depleted oil and gas fields. A preliminary investigation led to the selection of well TH75CX as the injection well near the No. 2 United Station (Fig. 2).

A 5500 m deep borehole site investigation revealed that the Ordovician stratigraphic sequence in the well includes the Lower-Middle Ordovician Yingshan Group (O_{1-2y}). The Yingshan Group is the main oil and gas reservoir with a thickness of 51 m. As a carbonate rock reservoir, it mainly consists of open platform facies limestone. At present, the carbonate rock reservoir is in the end period of production and is considered the potential disposal site of acid gas.

3 Numerical approach

3.1 Numerical toolbox

A numerical simulation of this study was performed by the TMVR-EOSG (unpublished) simulator, which was developed from TMVOC-REACT (Zheng *et al.*, 2010, 2013). As with TMVOC-REACT, the simulator links TMVOC (Pruess and Battistelli, 2002) and TOUGHREACT (Xu *et al.*, 2012) by replacing the fluid and heat flow parts in TOUGHREACT with TMVOC. To analyze the coupling process occurring between flow and chemistry, gas partial pressures and fugacity coefficients calculated by the flow module (TMVOC) are passed to the geochemical module (TOUGHREACT). The routine GASEOS (Reagan, 2006) is also incorporated to calculate gas partial pressures and fugacity coefficients in gas mixtures. Temporal changes in porosity and permeability owing to mineral dissolution and precipitation are fed back to the fluid flow module by lagging one-time steps. Moreover, TMVR-EOSG additionally incorporates a new Equation of State (EOS), namely, Ziabakhsh-Ganji and Kooi EOS (Ziabakhsh-Ganji and Kooi, 2012) with binary interaction coefficients for CO_2–SO_2, CO_2–H_2S, CO_2–CH_4 and CO_2–N_2. The new EOS can simulate the impacts of gas mixtures including CO_2, SO_2, H_2S, CH_4 and N_2, and allow for an accurate and efficient modeling of the thermodynamic equilibrium of gas mixtures and brines.

3.2 Model setup

To investigate the potential physical and geochemical interactions occurring among acid gas, formation water, and rock minerals, a one-dimensional (1D) radial model

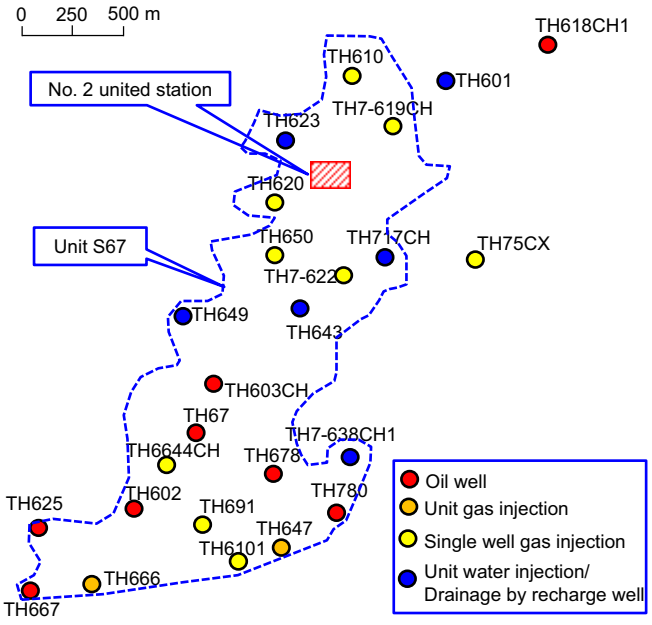

Fig. 2. The potential area for acid gas reinjection.

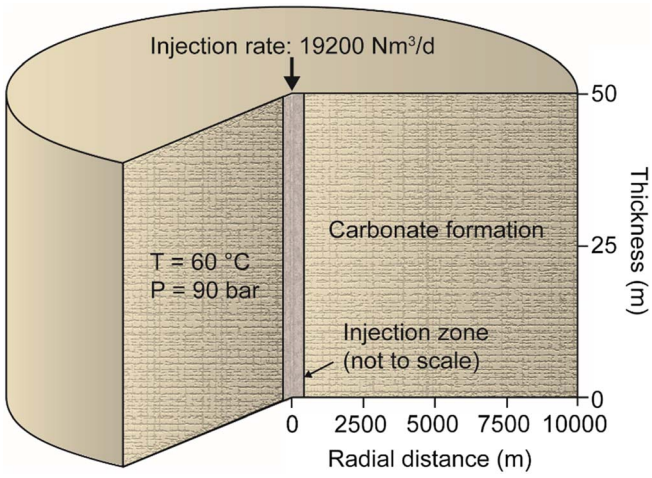

Fig. 3. Schematic diagram of the 1D radial model.

(Fig. 3) was used in the simulation. According to the underground conditions of the Yingshan Group, the 1D model was set as a homogeneous carbonate formation with a thickness of 50 m. In the lateral direction, the model covered a 10 000 m radial distance and 130 radial grid elements with the grid spacing gradually increasing away from the injection well. The volume of the outer grid element is specified as a large value of 10^{30} m^3 to represent an infinite lateral extent.

Based on the acid gas injection project designed by the *SINOPEC*, the acid gas injection rate is 19 200 Nm^3/d for 25 years. The original flue gas generated by the No. 2 United Station includes 0.19 mol% methane (CH_4), 0.05 mol% ethane (C_2H_6), 0.03 mol% propane (C_3H_8), 1.47 mol% nitrogen (N_2), 46.77 mol% CO_2, 42.3 mol% H_2S and 9.2 mol% water (H_2O). Multistage pressurization and dehydration caused water extraction prior to acid gas injection. The total percentage for CH_4, C_2H_6, C_3H_8 and N_2 is just 1.92 mol%, and thus, only CO_2 and H_2S are the dominant components considered in our numerical simulation.

Acid gas was injected at a constant rate of 0.229 kg/s for CO_2 and 0.160 kg/s for H_2S in the simulation. In the simulation, a continuous gas injection was applied for a period of 25 years, and the geochemical transport simulations were run for 10 000 years.

3.3 Initial conditions

The initial reservoir pressure is 600 bar, and the formation temperature is 128 °C at a depth of 5500 m. However, due to limitations of existing studies, the experimental data for H_2S solubility were within a relatively high temperature (321 °C) and low pressure (210 bar) (Zheng *et al.*, 2010). As a result, the simulator is applicable at moderate temperatures (< 200 °C) and pressures (< 200 bar). The convergence will probably worsen if the simulation is run under high-temperature and high-pressure conditions. More importantly, the accuracy of the calculation will decrease, because the solubility of a component present in different phases that is currently implemented in TMVR-EOSG is only valid under low temperature and pressure (Zheng *et al.*, 2010, 2013). According to the phase-equilibrium properties of the system (Bierlein and Kay, 1953), the critical temperature and critical pressure are approximately 57 °C and 82 bar, respectively. To ensure the supercritical state of acid gas, the pressure and temperature are set as 90 bar and 60 °C in the simulation, respectively.

The initial mineral composition was derived from laboratory studies of the Yingshan Group carbonate by X-Ray Diffraction (XRD) analysis. The reservoir comprises 97% volume calcite and 3% volume quartz. The hydrogeologic parameters used in the 1D radial model are listed in Table 1. Petrophysical properties such as porosity and permeability of rock formations were inferred from the statistical data summarized in the literature (Liang *et al.*, 2016). The evaluation index for porosity is the cumulative amount of single well oil production (Tab. 2). Since the oil production of TH75CX is 13 668 t, the porosity is set at 0.2. The permeability is assumed to be the average value of 5×10^{-12} m^2 in the simulation. Due to the lack of available data, other required hydrogeological parameters are specified according to the literature (Xu *et al.*, 2007; Zhang *et al.*, 2011).

Water chemical analysis results are available for the water samples taken from the injection well TH75CX. The Yingshan Formation water is dominated by $CaCl_2$, and the aqueous solution composition is shown in Table 3.

3.4 Kinetic parameters of mineral dissolution and precipitation

The reversible and fast geochemical reactions can be described properly by the chemical equilibrium model. However, a kinetic model is necessary to represent irreversible

Table 1. Hydrogeological parameters for the 1D radial model.

Parameters	Value
Permeability (m^2)	5×10^{-12}
Porosity	0.2
Tortuosity	0.3
Pore compressibility (Pa^{-1})	1×10^{-8}
Diffusivity (m^2/s)	1×10^{-9}
Rock grain density (kg/m^3)	2600
Rock grain specific heat (J/(kg °C))	920
Formation heat conductivity (W/(m °C))	2.51
Relative permeability model	
Liquid (van Genuchten): $k_{rl} = \sqrt{S^*}\left\{1 - \left(1 - [S^*]^{1/m}\right)^m\right\}^2$	$S^* = (S_l - S_{lr})/(1 - S_{lr})$
S_{lr}: residual water saturation	$S_{lr} = 0.30$
m: exponent	$m = 0.457$
Gas (Corey):	
$k_{rg} = \left(1 - \hat{S}\right)^2\left(1 - \hat{S}^2\right)$	$\hat{S} = (S_l - S_{lr})/(S_l - S_{lr} - S_{gr})$
S_{gr}: residual gas saturation	$S_{gr} = 0.05$
Capillary pressure model (van Genuchten)	
$P_{cap} = -P_0\left([S^*]^{-1/m} - 1\right)^{1-m}$	$S^* = (S_l - S_{lr})/(1 - S_{lr})$
S_{lr}: residual water saturation	$S_{lr} = 0.00$
m: exponent	$m = 0.457$
P_0: strength coefficient (kPa)	$P_0 = 19.61$

Table 2. Porosity in the carbonate reservoir of the Tahe oilfield, Xinjiang, China.

Cumulative oil production (N_p)	Porosity (%)
$N_p > 15 \times 10^4$ t	50~60
4.5×10^4 t $< N_p < 15 \times 10^4$ t	30~40
$N_p < 4.5 \times 10^4$ t	20

heterogeneous reactions, for instance, mineral carbonation (Marini, 2006). A kinetic model is adopted by TOUGHREACT based on the transition state theory, where the kinetic rate is expressed as (Lasaga *et al.*, 1994):

$$r_n = \pm k_n A_n |1 - \Omega_n^{\theta}|^{\eta} \quad (1)$$

where r_n is the kinetic rate (positive values denote mineral dissolution and negative values denote precipitation), k_n is the kinetic rate constant (mol m^{-2} s^{-1}), A_n is the specific surface area (m^2 kg w^{-1}), and Ω_n is the kinetic mineral saturation ratio. The parameters θ and η are set to one in this study as in common practice.

The kinetic rate constant k_n is influenced not only by temperature, but also by different chemistry mechanisms (acid, neutral and base mechanisms). For many minerals,

Table 3. Initial water chemistry of the Yingshan Formation, Xinjiang area, China.

Component	Concentration (mol/L)
Na^+	2.580×10^{-1}
Ca^{2+}	1.602×10^{-1}
Mg^{2+}	5.165×10^{-3}
Cl^-	3.315×10^{-1}
HCO_3^-	4.076×10^{-4}
SO_4^{2-}	1.821×10^{-4}
$SiO_{2(aq)}$	4.570×10^{-4}
pH	6.8

the kinetic rate constant k_n is summarized as (Lasaga *et al.*, 1994; Palandri and Kharaka, 2004):

$$k_n = k_{25}^{nu} \exp\left[\frac{-E_a^{nu}}{R}\left(\frac{1}{T} - \frac{1}{298.15}\right)\right] + k_{25}^{H} \times \exp\left[\frac{-E_a^{H}}{R}\left(\frac{1}{T} - \frac{1}{298.15}\right)\right] a_H^{n_H} + k_{25}^{OH} \times \exp\left[\frac{-E_a^{OH}}{R}\left(\frac{1}{T} - \frac{1}{298.15}\right)\right] a_{OH}^{n_{OH}} \quad (2)$$

Table 4. Kinetic parameters for minerals.

Mineral	A' (cm^2/g)	Parameters for the kinetic rate law							
		Neutral mechanism		Acid mechanism			Base mechanism		
		k_{25} ($mol/m^2/s$)	E_a (kJ/mol)	k_{25} ($mol/m^2/s$)	E_a (kJ/mol)	n_H	k_{25} ($mol/m^2/s$)	E_a (kJ/mol)	n_{OH}
Calcite	9.8	1.549×10^{-6}	23.5	5.012×10^{-1}	14.4	1.0	3.311×10^{-4}	35.1	1.0
Quartz	9.1	1.023×10^{-14}	87.7						

where superscripts or subscripts nu, H, and OH indicate neutral, acid and base mechanisms, respectively. k_{25} is the rate constant at 25 °C, E_a is the activation energy, R is the gas constant, T is the absolute temperature, a is the activity of the species, and n is the power term (constant). The dissolution rate is assumed to be equal to the precipitation rate for all minerals. In this study, the parameters for the kinetics of dissolution and precipitation listed in Table 4 are taken from the literature (Marini, 2006; Zhu *et al.*, 2013).

In the geochemical reaction process, only a portion of the mineral surface can be dissolved. The surface area directly involved in mineral dissolution and precipitation by the solid unit mass is called the specific surface area. TOUGHREACT uses the following relationship to compute reactive surface areas of minerals (Xu *et al.*, 2012):

$$A_r = (V_{frac} A_m + A_{prc})/C_w \quad (3)$$

where A_r is the effective reactive surface area of minerals in units of $m^2_{mineral}/kg_{water}$ for input into the kinetic rate laws (Eq. (2)), A_m is the surface area in units of $m^2_{mineral}/m^3_{mineral}$, A_{prc} is the precursor surface area in units of $m^2_{mineral}/m^3_{medium}$, V_{frac} is the mineral volume fraction in $m^3_{mineral}/m^3_{medium}$ and C_w is the wetted-surface conversion factor in units of kg_{water}/m^3_{medium}. A_m, V_{frac} and C_w change during the course of a simulation as minerals dissolve and precipitate and as the liquid saturation of the medium fluctuates.

In terms of minerals in a rock, surface areas in units of cm^2/g can be calculated from

$$A' = 100/\rho_m = 100 A M_m / V_m \quad (4)$$

where A is the surface area in units of cm^2/g, ρ_m is the mineral density in g/cm^3, Mm is the molecular weight in mol/g, Vm is the molar volume in cm^3/mol, and A' is the specific reactive surface area specified in the simulation. In this study, A' used in the simulations is based on the literature (Xu *et al.*, 2007; Zhu *et al.*, 2013), as shown in Table 4.

As a result of mineral precipitation and dissolution, the volume of the matrix changes. In TOUGHREACT, porosity changes are directly tied to volume changes and taken in the code as follows (Xu *et al.*, 2012):

$$\phi = 1 - \sum_{m-1}^{nm} fr_m - fr_u \quad (5)$$

where nm is the number of minerals, fr_m is the volume fraction of mineral m in the rock ($V_{mineral}/V_{medium}$, including porosity), and fr_u is the volume fraction of the nonreactive rock. As the fr_m of each mineral changes, the porosity is recalculated at each time step.

Several options are available in TOUGHREACT to calculate permeability changes as a result of mineral precipitation and dissolution. In this study, it is assumed that permeability does not change during the course of simulation.

4 Results

4.1 Similarity solution of the simplified radial flow

In the numerical simulation, 1D radial flow, infinite and uniform aquifer, and constant injection rate were specified. Under these conditions, the results are expected to be self-similar and can be plotted against the similarity variable r^2/t. The self-similarity of the numerical results is a good method of assessing the space and time discretization (Pruess and García, 2002; Pruess and Müller, 2009). Figure 4 confirms that the gas saturation and pressure profiles at 1 year and 25 years are self-similar.

Figure 4 shows that there are two distinct regions. The inner region ($r^2/t < 1.35 \times 10^{-4}$ m^2/s) is a two-phase (liquid-gas) zone, and the outer region ($r^2/t > 1.35 \times 10^{-4}$ m^2/s) is a single-phase liquid condition. The maximum gas saturation is 0.27, which indicates that the injection of acid gas only partially displaces the resident formation brine. The minimum liquid saturation is 0.73. It is noted that the pressure change has the same transition point as the gas saturation at $r^2/t = 1.35 \times 10^{-4}$ m^2/s. The maximum pressure caused by acid gas injection is 90.28 bar. Pressure buildup occurs on a large scale when massive acid gas is injected into the formation, and the effect occurring in the two-phase zone is more pronounced than in the single-phase zone.

4.2 Acid gas migration

To better understand the process of acid gas migration, selected information is presented in graphical form as a function of radial distance from the injection wellbore at discrete time intervals of 0.01, 1, and 25 years during the injection period, and 100, 1000, and 10 000 years during the postinjection period. The evolution of gas saturation

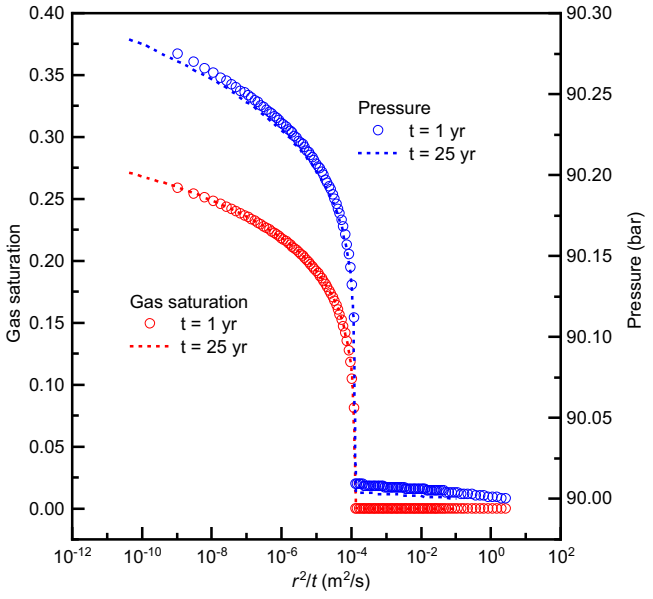

Fig. 4. Simulated gas saturation and pressure as a function of the similarity variable.

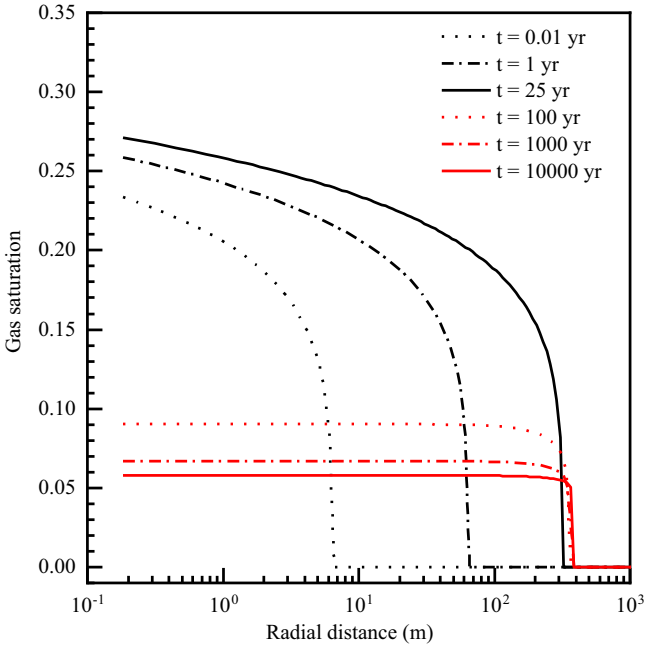

Fig. 5. Evolution of gas saturation at different times.

and mass fractions of the acid gas components (CO_2 and H_2S) in gas and aqueous phases is shown in Figures 5 and 6, respectively.

The formation is initially full of brine, and the injection of acid gas into the formation invades the pore space. Under the control of the pressure gradient and capillary forces, the resident brine located near the wellbore will be displaced and will migrate into the surroundings. The displacement is a drainage process in terms of the relevant displacement characteristics of acid gas and brine. The acid gas displacement fronts migrate approximately 6, 60, and 300 m at 0.01, 1, and 25 years, respectively, during injection, as shown in Figure 5; in the vicinity of the injection well, the maximum gas saturations reach 0.23, 0.26, and 0.27, respectively; correspondingly, the minimum liquid saturations during injection are 0.77, 0.74, and 0.73, respectively, which are much larger than the residual water saturation ($s_{lr} = 0.3$).

During the postinjection period, the main displacement is a mixing process of drainage and imbibition processes. On the one hand, acid gas migrates farther under the pressure gradient. At 100 years, the acid gas displacement front migrates approximately 343 m (Fig. 5). On the other hand, the capillary pressure serves as a driving force to induce a backflow of brine toward the injection point. In addition, the injected acid gas gradually dissolves in the formation water. Thus, the gas saturation decreases to 0.09 at 100 years. After 1000 years, the acid gas-displacement front stops progressing forward, and the main displacement occurring is the imbibition process. The system has a tendency to reach equilibrium when gas saturation decreases approximately to the residual gas saturation of 0.05.

The evolution of the CO_2 and H_2S mass fractions in the gas and aqueous phases at different times is shown in Figure 6. In terms of the mass fractions dissolved in the aqueous phase, the distances of the maximum CO_2 mass fraction are 6.6, 65.3, and 323.7 m at 0.01, 1, and 25 years, respectively, and those of H_2S are 4.1, 43.6, and 216.3 m at 0.01, 1, and 25 years, respectively, during injection. During the postinjection period, the distance of the maximum CO_2 mass fraction dissolved in the aqueous phase is 363.3 m at 100 years, and the distance of the maximum H_2S mass fraction dissolved in the aqueous phase at 100 years is 229.1 m. Because the acid gas displacement front does not progress forward after almost 1000 years (Fig. 5), the distances of the maximum CO_2 and H_2S mass fractions dissolved in the aqueous phase remain at 384.9 and 229.1 m, respectively. The maximum dissolved CO_2 mass fraction is achieved at a longer distance than that of the maximum dissolved H_2S mass fraction. In other words, the displacement distance of CO_2 is longer than H_2S in the aqueous phase at any time.

For the mass fraction in the gas phase, the changing process has similar characteristics to the mass fraction in the aqueous phase. The distances of the maximum CO_2 mass fraction are 6.6, 65.3, and 323.7 m at 0.01, 1, and 25 years, respectively, and those of H_2S are 3.453, 38.8, and 192.9 m at 0.01, 1, and 25 years, respectively, during injection. During the postinjection period, the distance of the maximum CO_2 mass fraction in the gas phase is 343 m at 100 years, and H_2S is 204.3 m. The distance of the maximum CO_2 mass fraction and H_2S in the gas phase remains at 363.3 and 204.3 m, respectively, after 1000 years. Thus, the displacement distance of CO_2 is longer than H_2S in the gas phase at any time.

Additionally, the maximum CO_2 mass fraction in the aqueous phase is 0.04, and then decreases to 0.023 when the H_2S mass fraction increases to 0.043. The results

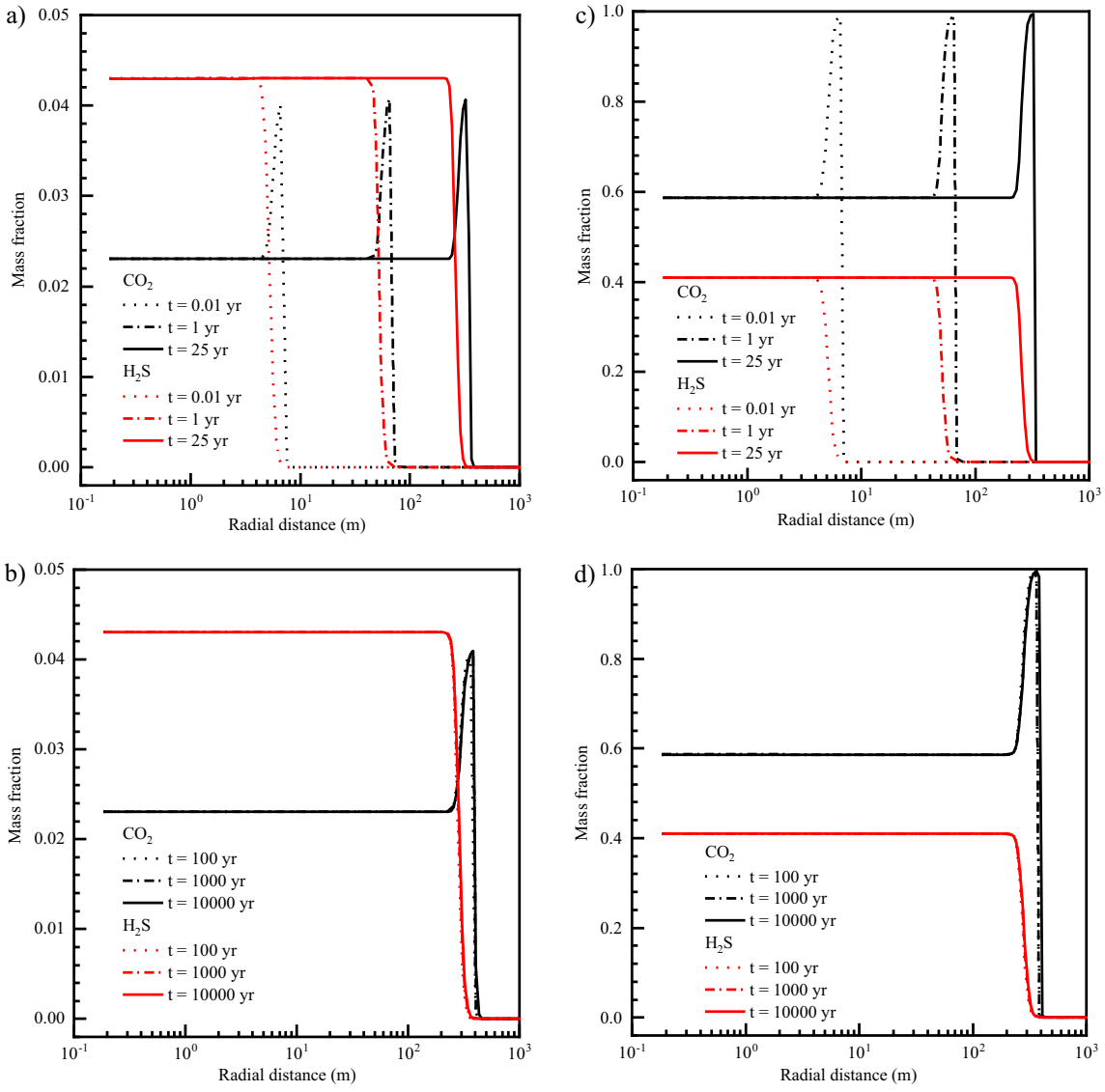

Fig. 6. Evolution of CO_2 and H_2S mass fractions (a) in the aqueous phase during injection, (b) in the aqueous phase during postinjection, (c) in the gas phase during injection, and (d) in the gas phase during postinjection.

indicate that the solubility of H_2S in formation water is two times higher than that of CO_2. In the gas phase, the maximum CO_2 mass fraction decreases from 1 to 0.59 (the CO_2 mass fraction in the injected acid gas) when the H_2S mass fraction increases to 0.41 (the H_2S mass fraction in the injected acid gas). This change occurs because there is a time lag in the breakthrough front between CO_2 and H_2S.

4.3 Pressure buildup

When acid gas is injected into deep formations, the invasion of acid gas in pore space will cause pressure buildup. Moreover, the pressure gradient that arises from acid gas injection has a tendency to drive acid gas to water-saturated pores. Thus, minor differences are observed in the evolution of pressure buildup (Fig. 7) and gas saturation (Fig. 5).

As with the evolution of gas saturation, pressure buildup has a significant increase at 6, 60, and 300 m, while acid gas is injected for 0.01, 1, and 25 years, respectively. The maximum pressure buildup is generated near the injection well at 0.25, 0.275, and 0.285 bar, respectively. However, an important difference is that pressure buildup is induced at a small value, although the gas saturation remains at zero before acid gas arrives.

During the postinjection time, pressure perturbations decrease gradually over time. The distance of sharp pressure buildup is 343 m at 100 years and then remains unchanged after 1000 years, which is in accordance with the distance of the gas displacement front. After 10 000 years, the pressure of the water-saturated region recovers to its original level, and the value of the two-phase region decreases to 0.08 bar.

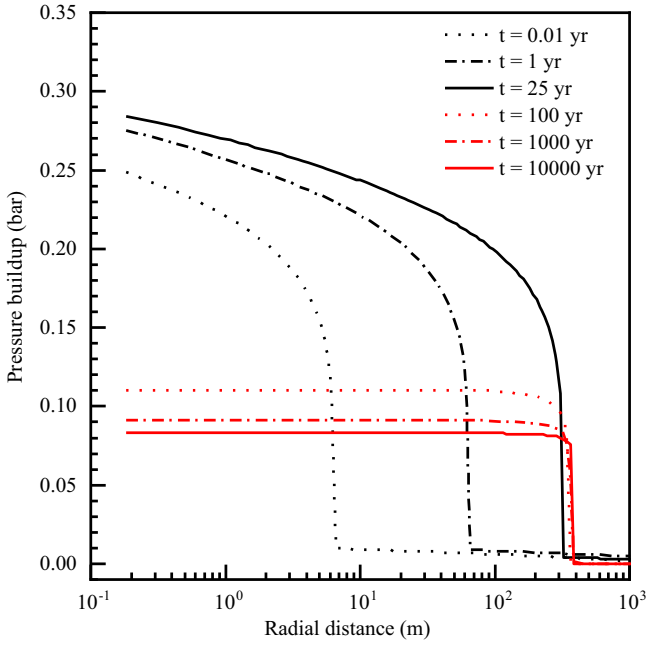

Fig. 7. Evolution of pressure buildup at different times.

4.4 Geochemical effects

After injection, acid gas dissolves in the formation water over time, and then undergoes hydrolysis reactions. For the acid gas system, those reactions and their associated equilibrium constants, $\log K_{25°C,1bar}$, are (Xu *et al.*, 2012):

$$CO_2(aq) + H_2O \leftrightarrow H^+ + HCO_3^- \log K_{25°C,1bar} =$$

$$\log([HCO_3^-][H^+]/([CO_2(aq)][H_2O])) = -6.58 \quad (6)$$

$$HCO_3^- \leftrightarrow H^+ + CO_3^{2-} \log K_{25°C,1bar} = -10.62 \quad (7)$$

$$H_2S(aq) \leftrightarrow HS^- + H^+ \log K_{25°C,1bar} = -7.42 \quad (8)$$

Reactions (6)–(8) all involve H^+ and then produce an acidic zone where the pH value tends to decrease. In a highly acidic environment, calcite may dissolve into formation water, consuming H^+ as subsequent reaction, which partially buffers the system:

$$CaCO_3 + H^+ \leftrightarrow Ca^{2+} + HCO_3^- \quad (9)$$

During acid gas injection, the distributions of HCO_3^- and HS^- concentrations in brine along the radial distance at different times are presented in Figure 8. Since pH value is the master variable in the system, we plot it as the right-hand axis on the plots.

As described above, the CO_2 transport distance is longer than the H_2S transport distance in the aqueous phase at each time. Together with Reactions (6)–(8), the HCO_3^- concentration increases rapidly to 0.93 mol/kg H_2O once the breakthrough front of CO_2 arrives. Then, due to the preferential dissolution of H_2S, the HCO_3^- concentration decreases gradually to 0.56 mol/kg H_2O as HS^- increases

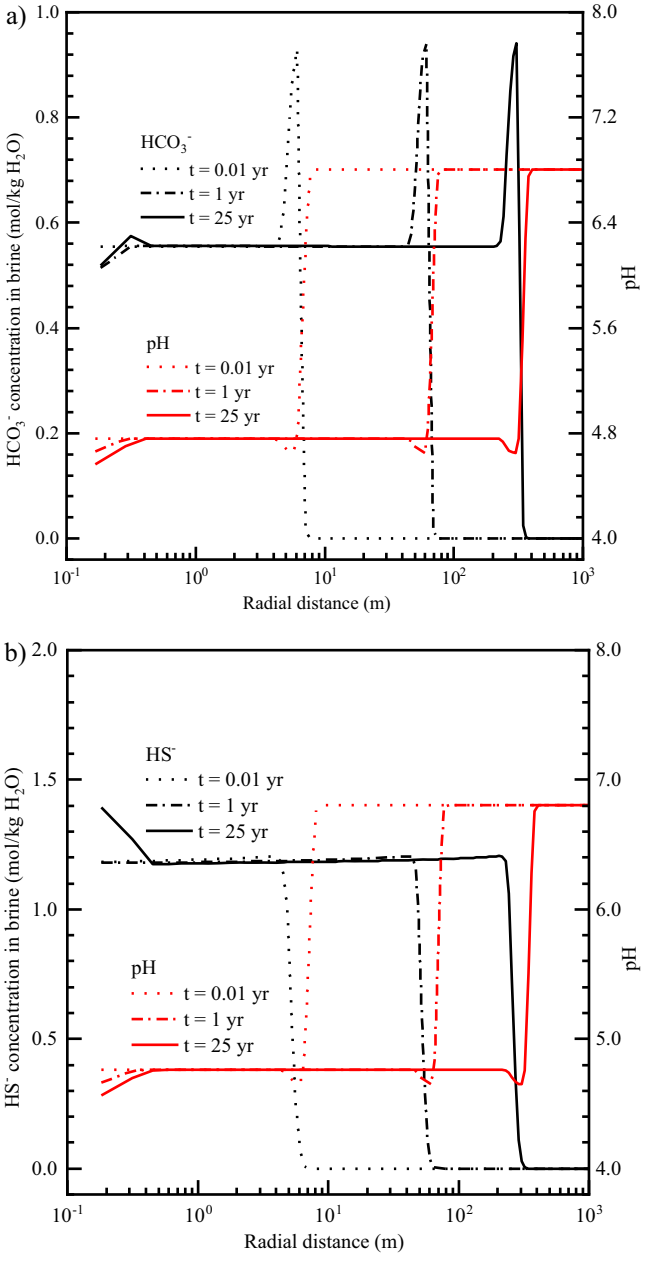

Fig. 8. Aqueous concentration and pH value at different times during the injection period.

to 1.17 mol/kg H_2O. The change in calcite abundance is so small (Fig. 10a) that the influence on pH value can be neglected. H_2S generates a weaker acidic solution than that of CO_2 since the equilibrium constant of Reaction (8) is smaller than that of Reaction (6). Consequently, the pH value decreases to 4.65 when the HCO_3^- concentration increases to the maximum value and subsequently increases to 4.76 due to the weaker acidity of H_2S.

In the region close to the injection well, a small amount of calcite precipitation occurs after 1 year, reaching a peak value of 1.6% at a distance of 0.32 m at 25 years. Calcite precipitation remains constant within a distance of 0.45 m after 25 years; thus, there is an overlap in that region

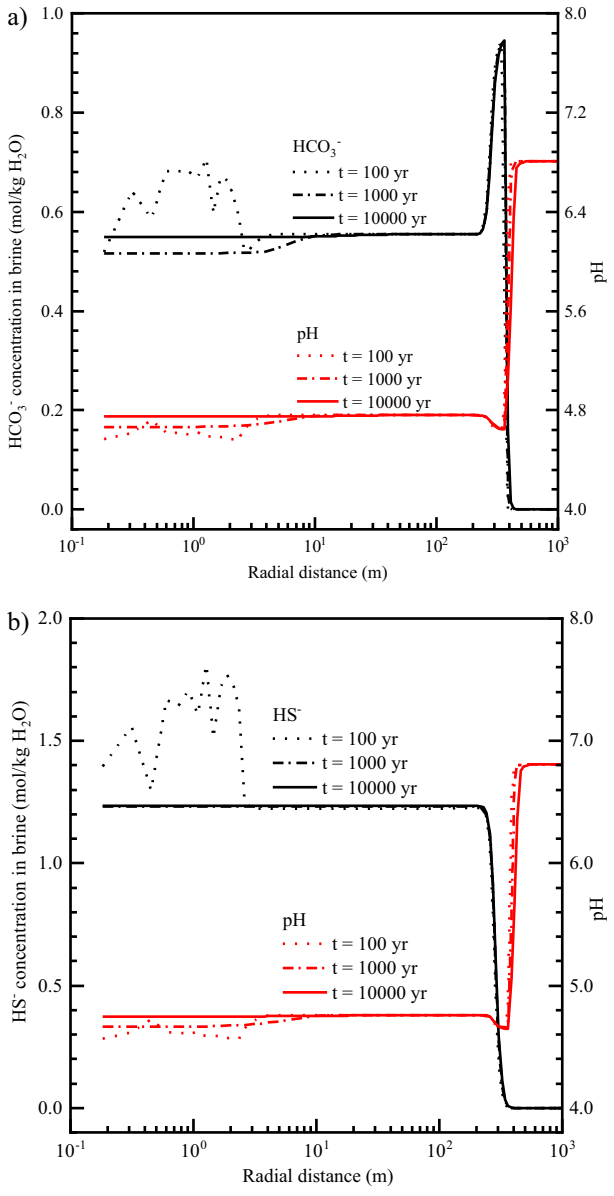

Fig. 9. Aqueous concentration and pH value at different times during the postinjection period.

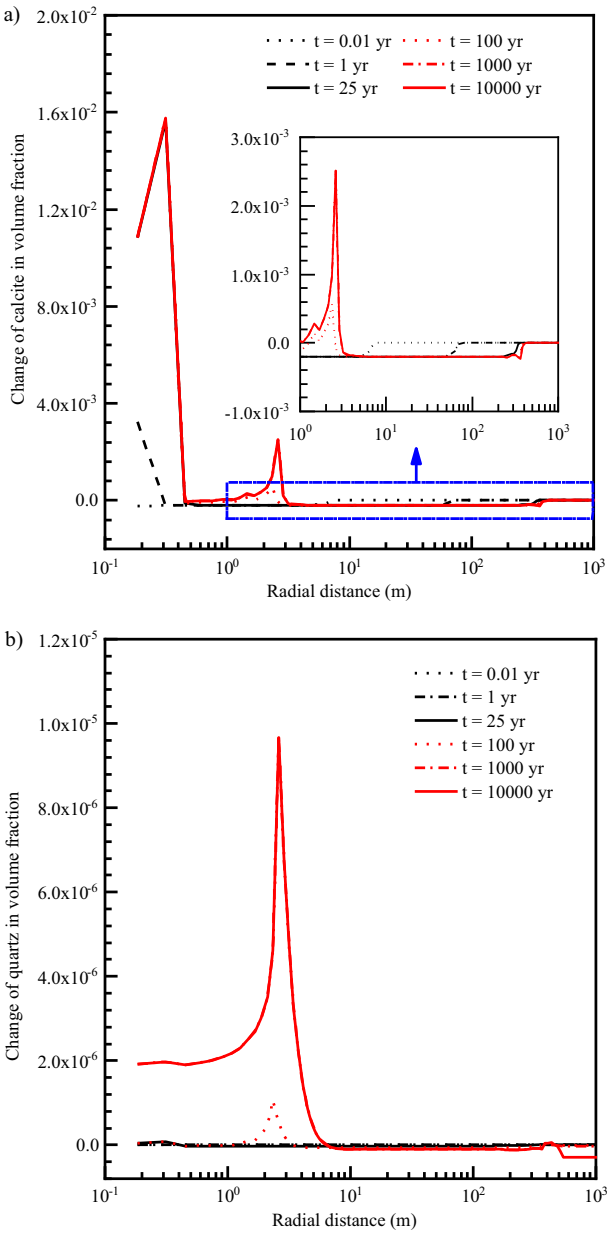

Fig. 10. Changes in (a) calcite and (b) quartz abundances at different times.

among the four curves of 25, 100, 1000, and 10 000 years (Fig. 10a). The reverse process of Reaction (9) has a tendency to generate H^+ and lower the pH value. At 25 years, the HCO_3^- concentration reaches 0.52 mol/kg H_2O and that of HS^- reaches 1.39 mol/kg H_2O when the injection ceases. A pH of approximately 4.57 is attained.

For the acid gas postinjection period, as shown in Figure 9, the distributions of HCO_3^- and HS^- concentrations in the region of the displacement front are very similar to those during the injection period. The pH value and calcite dissolution also increased. However, in the area close to the injection well, the calcite precipitation region extends to a radius of 2.6 m (the curves at 10 000 years coincide with those at 1000 years on the whole domain). Correspondingly, at 100 years, the HCO_3^- and HS^- concentrations increase significantly, and the pH value slightly decreases in that region. After that, the aqueous HCO_3^- and HS^- concentrations decrease to 0.55 mol/kg H_2O and 1.23 mol/kg H_2O, respectively. Moreover, a pH of approximately 4.75 is attained.

Only a marginal increase in quartz content can be observed in Figure 10b, with a peak volume fraction of 10^{-5} at a distance of approximately 2.6 m (the curve at 10 000 years coincides with that at 1000 years). Additionally, the precipitation and dissolution amount of calcite are relatively small. Therefore, the variation in porosity is rather small after acid gas injection, as shown in Figure 11. There are irrelevant porosity changes in regard to the hydraulic or mechanical properties of the reservoir.

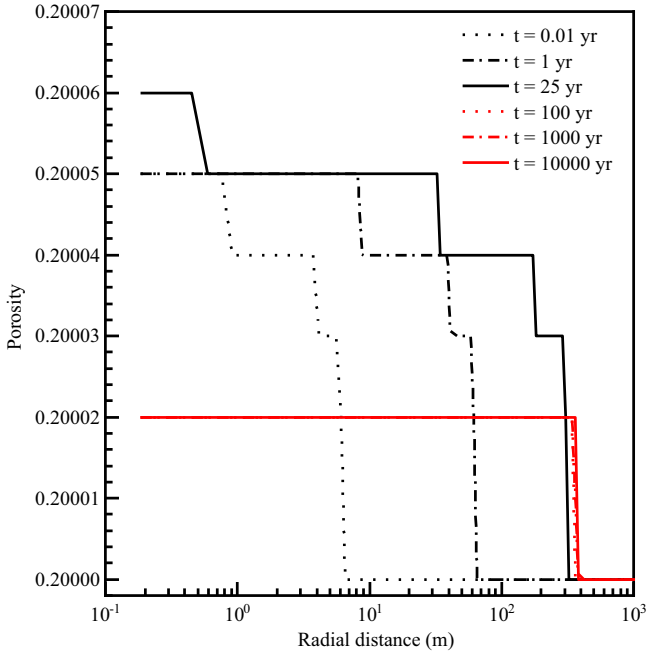

Fig. 11. Evolution of porosity at different times.

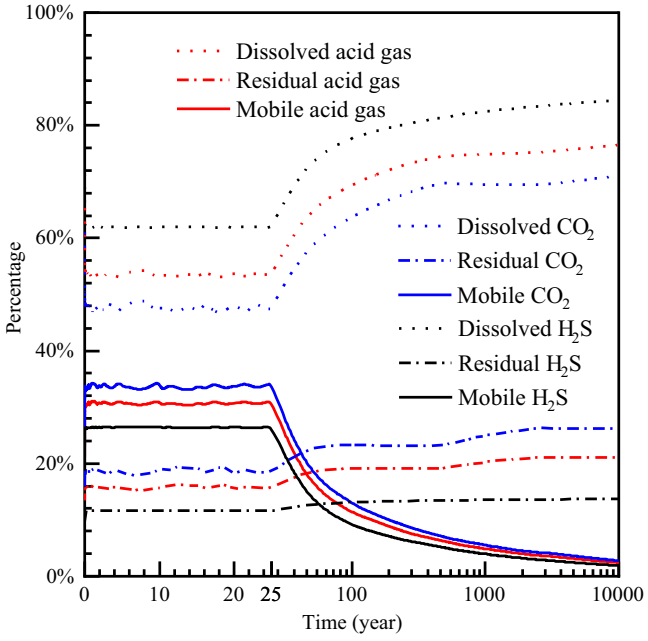

Fig. 12. Evolution of CO_2, H_2S and acid gas trapping at different times.

Furthermore, the area where porosity varies is consistent with that of the acid gas plume. The irrelevant porosity change is probably a consequence of numerical oscillation.

4.5 Acid gas trapping evolution

As with the CO_2 trapping mechanism, the acid gas trapping mechanism can be divided into geological trapping, geochemical trapping and hydrodynamic trapping (De Silva *et al.*, 2015; Talman, 2015). Geological trapping includes structural trapping and residual trapping, *i.e.*, mobile acid gas trapped by the formation structure or caprock units and by capillary pressure forces in the pore space. Geochemical trapping is composed of dissolution trapping and mineral trapping, and is thus considered to be a secure trapping mechanism because acid gas can be permanently stored in the formation without leaking to the surface.

For the simulated case, calcite dissolution occurs in the acidic zone, which is caused by the hydrolysis reactions of CO_2 and H_2S in the region of the displacement front. Therefore, no CO_2 or H_2S is sequestered in mineral phases during the displacement process; instead, some CO_2 and H_2S are dissolved. Although calcite is precipitated near the injection well, the amount of precipitation is almost equivalent to that of dissolution. As a result, no CO_2 mineral sequestration occurs after acid gas injection. Similarly, no H_2S mineral sequestration occurs after acid gas injection. Thus, there are three trapping mechanisms for acid gas, including mobile gas trapping, residual gas trapping and dissolution trapping, as shown in Figure 12.

During acid gas injection, the ratio of dissolved to total injected H_2S remains at 62%. In contrast, the ratio of dissolved to total injected CO_2 fluctuates from 46% to 49%, respectively. The variation in dissolution trapping is in line with that of the distribution of HCO_3^- and HS^- concentrations at different times during the injection period shown in Figure 8, which is a result of the preferential dissolution of H_2S over CO_2. As a result, the ratio of dissolved to total injected acid gas fluctuates from 53% to 54%, respectively. Similarly, 11.6% of H_2S is residually trapped, 18%~19% of CO_2 is residually trapped, and 15%~16% of acid gas is thus residually trapped during acid gas injection.

For the acid gas postinjection period, both the residual trapping and dissolution trapping gradually increase, as shown in Figure 12. After a 1000-year storage period, the percentages of dissolution trapping, residual trapping and mobile gas phases for H_2S are 84.8%, 13.7%, and 1.5%, respectively, and those for CO_2 are 71.0%, 2.7%, and 26.3%, respectively. Additionally, the percentages of total acid gas injection in solubility trapping, residual trapping and mobile gas trapping are 76.5%, 21.1%, and 2.4%, respectively.

4.6 Sensitivity analysis

To investigate the numerical model sensitivity to the reservoir parameters porosity, permeability and injection rate, six different cases were considered based on the reservoir parameters. In the first two cases, we changed the injection rate from 19 200 Nm^3/d (Base Case) to 38 400 Nm^3/d (Case 1) and to 9600 Nm^3/d (Case 2). According to the acid gas composition of the project, acid gas mixtures were injected at a constant rate of 0.458 kg/s CO_2 + 0.320 kg/s H_2S in Case 1 and 0.1145 kg/s CO_2 + 0.080 kg/s H_2S in Case 2. In Cases 3 and 4, the permeability values were changed from 5×10^{-12} (Base Case) to 5×10^{-11} (Case 3) and to 5×10^{-13} (Case 4). Finally, two cases with different

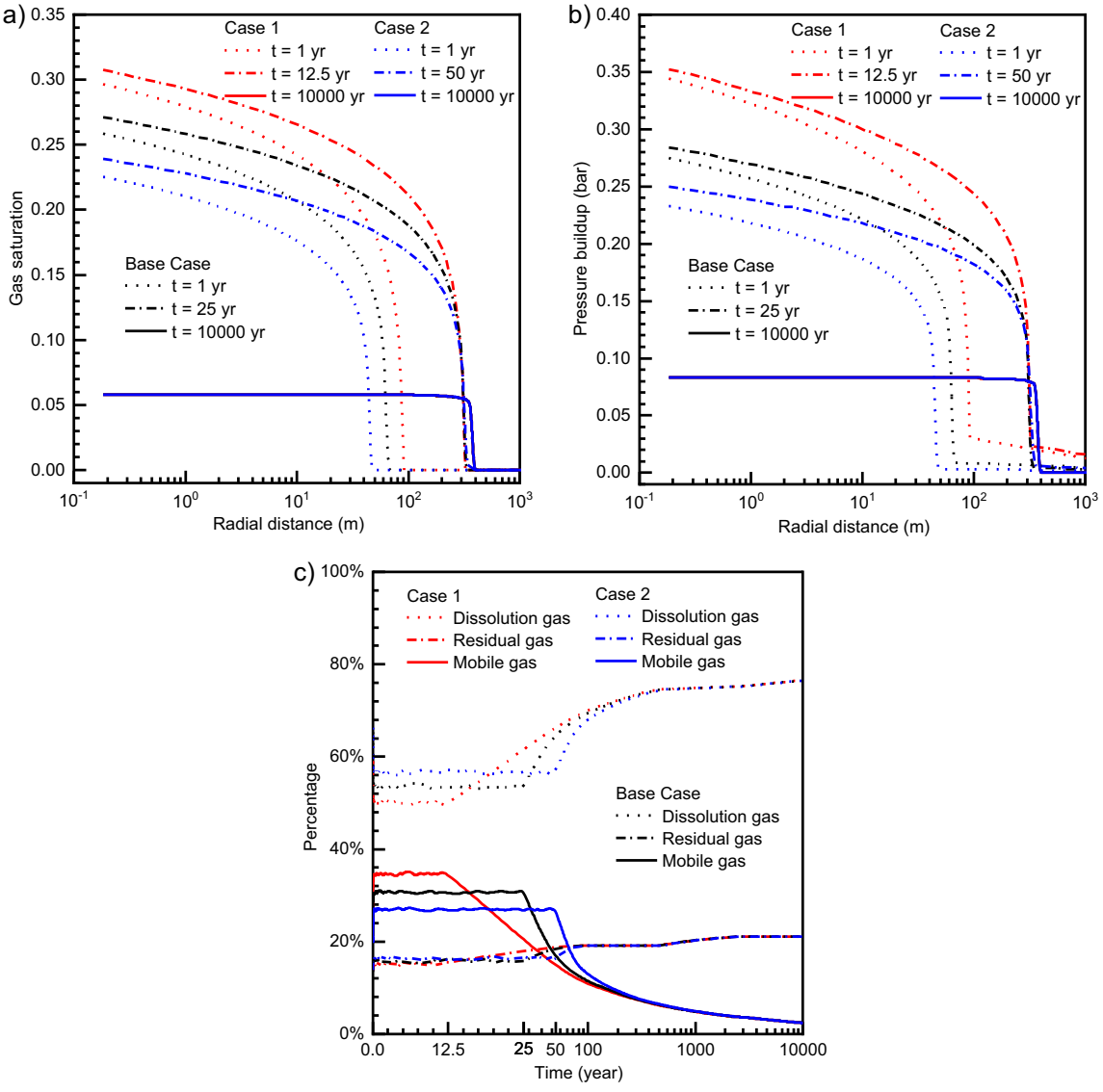

Fig. 13. Effect of injection rate on the (a) gas saturation, (b) pressure buildup at the three selected times and (c) the evolution of acid gas trapping. Note that gas saturation and pressure buildup coincide at 10 000 years for the three cases (where Base case, Case 1 and Case 2 indicate that the injection rate values are 0.229 kg/s CO_2 + 0.160 kg/s H_2S, 0.458 kg/s CO_2 + 0.320 kg/s H_2S and 0.1145 kg/s CO_2 + 0.080 kg/s H_2S, respectively).

porosities, 0.1 and 0.3, were performed (Cases 5 and 6, respectively). The total volume of acid gas injected in the reservoir is equivalent. Thus, the injection times of Case 1 and Case 2 are changed to 12.5 years and 50 years, respectively. In all other cases (Cases 3–6), the injection time was set as a value of 25 years, which was the same as the Base Case. Furthermore, in all cases, the time of geochemical transport simulations was set to 10 000 years.

Figure 13 shows the effect of the injection rate on the gas saturation and pressure buildup at three selected times as well as the evolution of acid gas trapping. The selected times include 1 year during the injection period and 10 000 years during the postinjection period in the three cases. The third selected times are 25, 12.5 and 50 in the Base Case, Case 1 and Case 2, respectively. Figure 13a shows that the gas saturation and migration distance increase during the injection period as the injection rate increases. At the end of acid gas injection, gas saturation is higher with a higher injection rate. However, the migration distances are almost the same. At 10 000 years, both the gas saturation and migration distances are the same at the three injection rates. The effect of the injection rate on the pressure buildup is consistent with that of the gas saturation (Fig. 13b). In terms of acid gas trapping, the percentage of dissolution trapping is smaller during the injection period when the injection rate is increased (Fig. 13c). However, the dissolution trapping rate is relatively higher after injection occurs at a higher injection rate.

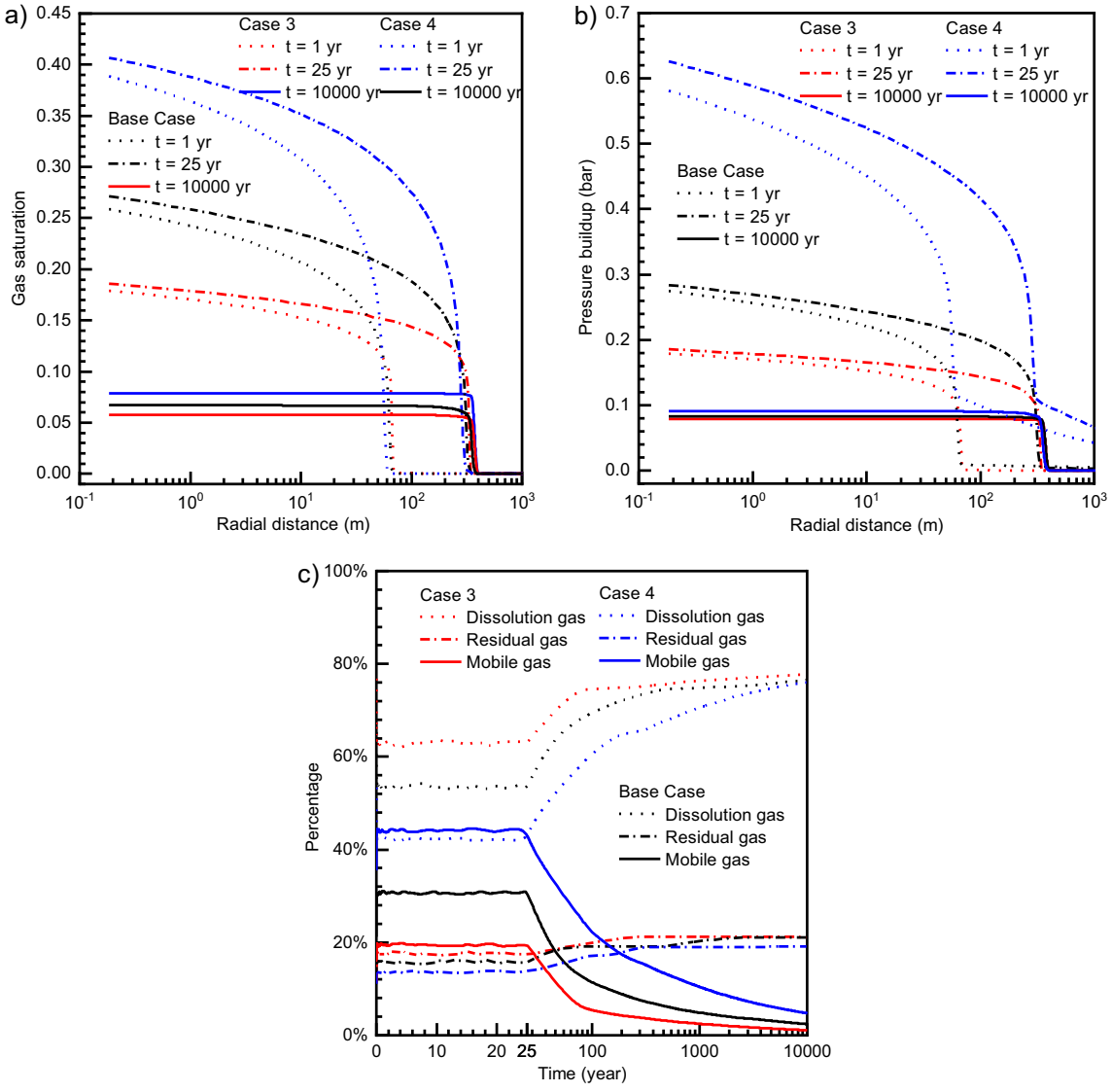

Fig. 14. Effect of permeability on the (a) gas saturation, (b) pressure buildup at the three selected times and (c) the evolution of acid gas trapping (where Base case, Case 3 and Case 4, indicate that the permeability values are 5×10^{-12}, 5×10^{-11} and 5×10^{-13}, respectively).

The differences in the rate of dissolution trapping for the different injection rates result from the differences in saturation distributions observed at the end of acid gas injection. At higher injection rates, much more acid gas is in the free gas phase. At 10 000 years, the same amounts of dissolution trapping are reached at the three injection rates. As shown in Figure 13c, the injection rate has little effect on the residual trapping.

Figure 14 illustrates the effect of permeability on the gas saturation and pressure buildup at three selected times as well as the evolution of acid gas trapping. Gas saturation, pressure buildup and acid gas trapping are significantly affected by permeability. Acid gas will be able to flow through more easily with a higher permeability. Thus, with a higher permeability, the gas saturation is lower and the migration distance is farther. The farther migration distance leads to a larger contact volume between the acid gas and formation water. As a consequence, the dissolution trapping ratio is relatively high at the end of the simulation with high permeability (Fig. 14c). The effect of permeability on pressure buildup is consistent with gas saturation and migration distance (Fig. 14b).

Figure 15 reports the effect of porosity on the gas saturation and pressure buildup at three selected times as well as the evolution of acid gas trapping. Acid gas moves farther when the porosity is reduced (Fig. 15a). The porosity has little effect on the gas saturation and pressure buildup. Additionally, as shown in Figure 15c, the same

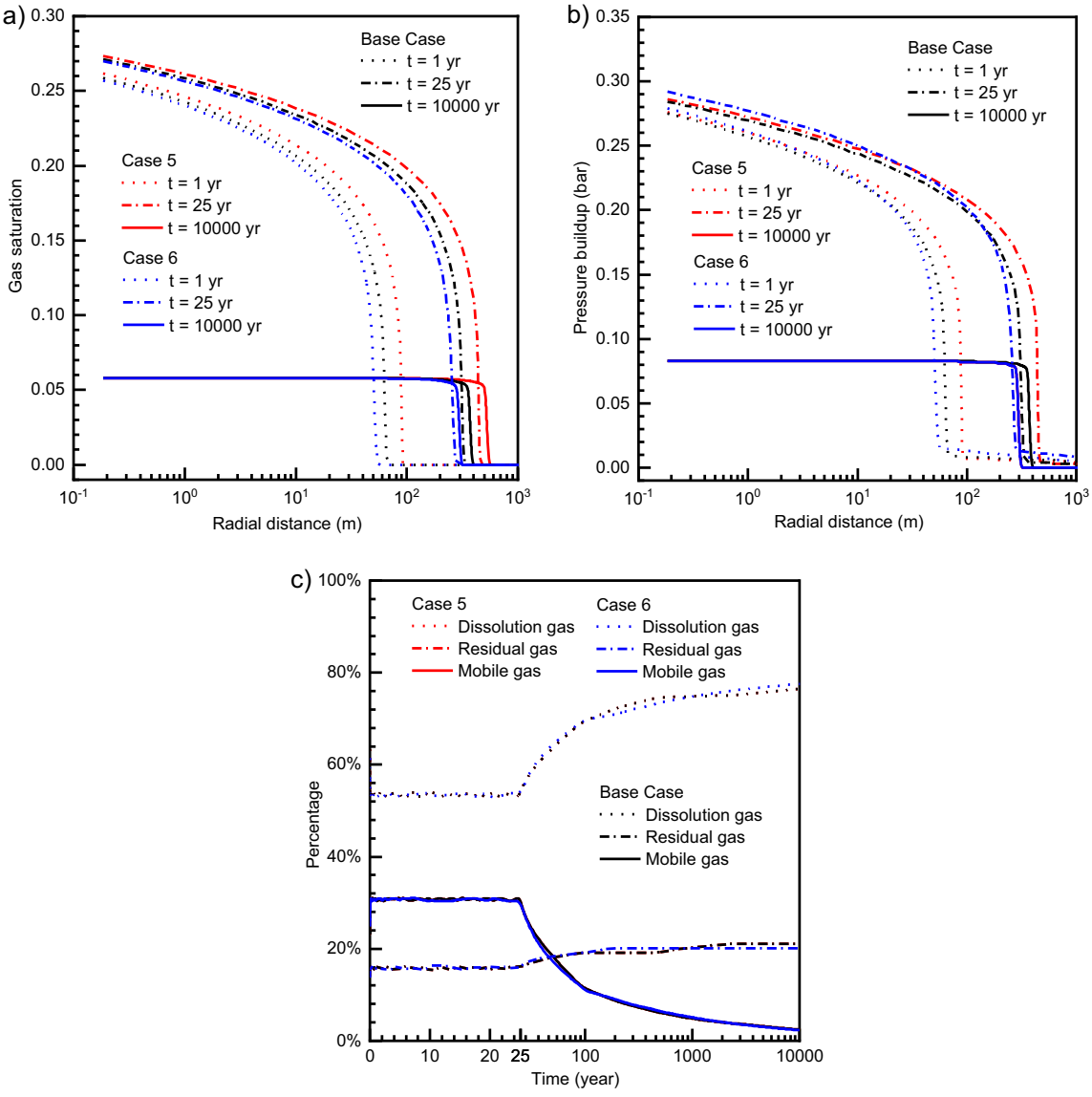

Fig. 15. Effect of porosity on the (a) gas saturation, (b) pressure buildup at the three selected times and (c) the evolution of acid gas trapping. Note that the acid gas trapping curves for Case 5 coincide with those for the Base Case (where Base case, Case 5 and Case 6 indicate that the values of porosity are 0.2, 0.1 and 0.3, respectively).

amounts of dissolution trapping are reached at the three porosities after acid gas injection.

5 Discussion

As investigated in the literature (Meng *et al.*, 2015; Pruess and García, 2002; Pruess and Müller, 2009; Zhao and Cheng, 2017), salt precipitation is caused at the dry-out region near the injection well where liquid saturation is lower than the residual water saturation. The formation porosity and permeability may be reduced by solid salt precipitation. Injectivity impairment will eventually occur after salt accumulation. Under the condition of acid gas injection in this study, the minimum liquid saturation is 0.73, which is much larger than the residual water saturation ($S_{lr} = 0.3$). Thus, there is no dry-out region observed in the reservoir. More importantly, the distribution of liquid saturation is beneficial to engineering operations.

After acid gas injection, the evolution of the CO_2 and H_2S mass fractions in the gas and aqueous phases indicates that the leading gas front consists of CO_2 due to the preferential dissolution of H_2S in the aqueous phase. This partitioning phenomenon is consistent with current research (Bachu and Bennion, 2009; Bachu *et al.*, 2009; Zhang *et al.*, 2011; Zheng *et al.*, 2010, 2013). In engineering operations, the quicker breakthrough of CO_2 can provide an advanced warning of a potential breakthrough of acid gas. Thus, immediate action should be taken once pure CO_2 is detected along the potential leakage pathway.

The pressure buildup region extends further than that of the acid gas plume, which is in agreement with existing research results (Birkholzer *et al.*, 2009; Liu *et al.*, 2018; Meng *et al.*, 2015). In response to acid gas injection, the fluid pressure in the storage formation reached maximum values of approximately 0.285 bar near the injection zone. According to current practices for the underground injection control of liquid wastes, the maximum allowable injection-induced pressure increase should be limited to reduce the risks of seismic events and geomechanical damage (Bandilla and Celia, 2017; Birkholzer *et al.*, 2009, 2015; Zhou *et al.*, 2010). For example, the regulated injection pressure is limited to 0.181 bar/m in the Illinois Basin. Correspondingly, the allowable pressure increase needs to be less than 65% of the preinjection pressure (Bandilla and Celia, 2017; Zhou *et al.*, 2010). In comparison, the maximum pressure buildup of 0.285 bar that was observed in the simulation corresponds to 0.32% of the preinjection pressure. Consequently, the pressure buildup due to acid gas injection is insignificant to the reservoir.

Only a small increase in quartz is observed after acid gas injection because quartz is relatively stable at pH values of 2.0–8.5 and below 250 °C (Li *et al.*, 2016; Xu *et al.*, 2007). In addition, the amounts of calcite precipitation and dissolution are relatively small. Consequently, the porosity is almost unaffected by chemical reactions.

Carbonate rocks have little trapping capacity for CO_2 because equilibrium is reached quickly from the accumulation of Ca^{2+} and HCO_{3^-} ions through congruent reactions (Gunter *et al.*, 2000; Zhu *et al.*, 2013). In fact, no CO_2 mineral sequestration occurred after acid gas injection in this study. When H_2S is injected into iron-rich formations, mineral trapping of H_2S is achieved after pyrite reactions occurred (Li *et al.*, 2016; Talman, 2015; Xu *et al.*, 2007). Due to the lack of iron-rich formations in carbonate reservoirs, mineral reactions induced by H_2S are not considered and no observed H_2S mineral sequestration occurs after acid gas injection. Eventually, there are three trapping mechanisms for acid gas including mobile gas trapping, residual gas trapping and dissolution trapping.

During acid gas injection, the gas saturation and pressure buildup increased considerably with increasing injection rate. As a result, the percentage of the mobile gas phase is larger at a higher injection rate. However, the rate of the mobile gas phase reduced to a minimum is higher. Thus, the injection rate can be increased to facilitate acid gas trapping, which could be used as guidance for acid gas injection.

In the present study, only a 1D model is considered for simplicity in the numerical simulations. In the future, a fully 3D model will be needed for practical storage scenarios.

6 Conclusion

The possible impact of acid gas injection has been successfully evaluated through numerical modeling of a conceptual model with the hydrologic properties and mineral compositions of the target Tarim Basin reservoir, the possible impact of acid gas injection has been successfully evaluated. The major conclusions are as follows:

1. The maximum gas saturation of 0.27 is achieved at the end of injection, which is beneficial to engineering operations. At 10 000 years, the gas saturation tends to reach 0.05. In addition, the preferential dissolution of H_2S delays its breakthrough compared to that of CO_2 both in the gas and aqueous phases, and the maximum CO_2 mass fraction is almost 1. This finding has great implications for detecting and providing advanced warning of the potential leakage of acid gas.
2. During the injection period, the maximum pressure buildup is generated at 0.285 bar near the injection well at 25 years, and a slight increase in pressure is observed at the region where the acid gas has not yet arrived. After 10 000 years, 0.08 bar of pressure buildup is achieved within the distance at which acid gas arrives, and pressure is recovered to the original level out of that distance. The maximum pressure buildup of 0.285 bar that was observed in the simulation corresponds to 0.32% of the preinjection pressure. Consequently, the pressure buildup that occurred due to acid gas injection has little effect on the reservoir.
3. At the displacement front, the amount of calcite precipitation is small enough to neglect. The concentration of HCO_{3^-} first increases and then decreases due to the preferential dissolution of H_2S. Because H_2S generates a weaker acidic solution than CO_2, the pH value decreases to 4.65 and subsequently increases to 4.76. In the region close to the injection well, a small amount of calcite precipitation occurs during the acid gas injection, and thus, a minimum pH value of approximately 4.57 is attained. The calcite precipitation region near the injection well extends largely after the acid gas injection ceases, and thus, there is a slight reduction in pH value in that region at 100 years. At the end of the simulation, a pH of approximately 4.75 is attained. In addition, the variation in porosity is relatively small after acid gas injection due to the small changes in calcite and quartz in the volume fraction.
4. There are three trapping mechanisms: mobile gas trapping, residual gas trapping and dissolution trapping. As a secure trapping mechanism, the ratio of dissolved H_2S to total injected H_2S is higher than that of CO_2 during acid gas injection. At the end of acid gas injection, 54% of acid gas is trapped by dissolution trapping, and 76.5% is trapped at the end of simulation.
5. There is a higher rate of mobile gas phase decreasing to the minimum amount with a higher injection rate. The injection rate can be increased to facilitate acid gas trapping, which could be used as guidance for acid gas injection.
6. The porosity has little effect on the gas saturation, pressure buildup and trapping mechanism. However, gas saturation, pressure buildup and acid gas trapping are significantly affected by permeability. Under a higher permeability, the gas saturation is lower and

the migration distance is farther. Correspondingly, the mobile phase ratio is lower at the end of the simulation.

In summary, the distribution of acid gas is beneficial to acid gas injection. Moreover, the pressure buildup is under the allowable pressure increase. Additionally, the porosity change is negligible due to small changes in calcite and quartz in the volume fraction. In conclusion, our simulation indicates that acid gas injection is feasible in the carbonate formation of the Tarim Basin.

Acknowledgments. The authors wish to thank Prof. Simon Mathias of Durham University for his improvements in grammar and readability. The authors also wish to thank the two anonymous reviewers for their constructive suggestions for improving the quality of the manuscript. Special thanks to Guizhen Liu for her map illustration. This work was partially supported by the National Natural Science Foundation of China (Grant Nos. 41872210, 41274111) and SINOPEC Northwest Oilfield Branch (Grant No. 34400007-17-ZC0607-0172)

References

Bachu S., Bennion D.B. (2009) Chromatographic partitioning of impurities contained in a CO_2 stream injected into a deep saline aquifer: Part 1. Effects of gas composition and in situ conditions, *Int. J. Greenhouse Gas Control* **3**, 4, 458–467.

Bachu S., Gunter W.D. (2004) Overview of acid-gas injection operations in western Canada, *Seventh International Conference on Greenhouse Gas Control Technologies (GHGT-7), Vancouver, Canada*, pp. 1–6.

Bachu S., Pooladi-Darvish M., Hong H. (2009) Chromatographic partitioning of impurities (H_2S) contained in a CO_2 stream injected into a deep saline aquifer: Part 2. Effects of flow conditions, *Int. J. Greenhouse Gas Control* **3**, 4, 468–473.

Bacon D.H., Ramanathan R., Schaef H.T., Mcgrail B.P. (2014) Simulating geologic co-sequestration of carbon dioxide and hydrogen sulfide in a basalt formation, *Int. J. Greenhouse Gas Control* **21**, 2, 165–176.

Bandilla K.W., Celia M.A. (2017) Active pressure management through brine production for basin-wide deployment of geologic carbon sequestration, *Int. J. Greenhouse Gas Control* **61**, 155–167.

Bierlein J.A., Kay W.B. (1953) Phase-equilibrium properties of system carbon dioxide-hydrogen sulfide, *Ind. Eng. Chem.* **45**, 3, 618–624.

Birkholzer J.T., Oldenburg C.M., Zhou Q. (2015) CO_2 migration and pressure evolution in deep saline aquifers, *Int. J. Greenhouse Gas Control* **40**, 203–220.

Birkholzer J.T., Zhou Q., Tsang C.-F. (2009) Large-scale impact of CO_2 storage in deep saline aquifers: A sensitivity study on pressure response in stratified systems, *Int. J. Greenhouse Gas Control* **3**, 2, 181–194.

British Columbia Geological Survey (2003) *Acid gas injection: A study of existing operations phase I: Final report*, Ministry of Energy, Mines and Petroleum Resources, British Columbia Geological Survey, p. 71.

Cantucci B., Montegrossi G., Buttinelli M., Vaselli O., Scrocca D., Quattrocchi F. (2015) Geochemical barriers in CO_2 capture and storage feasibility studies, *Transp. Porous Media* **106**, 1, 107–143.

Carroll J.J., Griffin P.J., Alkafeef S.F. (2009) Review and outlook of subsurface acid gas disposal, in: *SPE Middle East Oil and Gas Show and Conference*, Society of Petroleum Engineers, Manama, Bahrain, p. 10.

Chen H., Yang S., Dong C., Zhu G., Jia C., Wei G., Wang Z. (1997) Geological thermal events in Tarim basin, *Chin. Sci. Bull.* **07**, 580–584.

De Silva G.P.D., Ranjith P.G., Perera M.S.A. (2015) Geochemical aspects of CO_2 sequestration in deep saline aquifers: A review, *Fuel* **155**, 128–143.

Gao Z., Liu Z., Gao S., Ding Q., Wu S., Liu S. (2016) Characteristics and genetic models of lower Ordovician carbonate reservoirs in southwest Tarim basin, NW China, *J. Pet. Sci. Eng.* **144**, 99–112.

Gunter W.D., Perkins E.H., Hutcheon I. (2000) Aquifer disposal of acid gases: Modelling of water–rock reactions for trapping of acid wastes, *Appl. Geochem.* **15**, 8, 1085–1095.

Jia L., Cai C., Jiang L., Zhang K., Li H., Zhang W. (2016) Petrological and geochemical constraints on diagenesis and deep burial dissolution of the Ordovician carbonate reservoirs in the Tazhong area, Tarim basin, NW China, *Mar. Pet. Geol.* **78**, 271–290.

Khan C., Amin R., Madden G. (2013) Effects of CO_2 and acid gas injection on enhanced gas recovery and storage, *Journal of Petroleum Exploration and Production Technology* **3**, 1, 55–60.

Knauss K.G., Johnson J.W., Steefel C.I. (2005) Evaluation of the impact of CO_2, co-contaminant gas, aqueous fluid and reservoir rock interactions on the geologic sequestration of CO_2, *Chem. Geol.* **217**, 3, 339–350.

Lasaga A.C., Soler J.M., Ganor J., Burch T.E., Nagy K.L. (1994) Chemical weathering rate laws and global geochemical cycles, *Geochim. Cosmochim. Acta* **58**, 10, 2361–2386.

Li C., Zhang F., Lyu C., Hao J., Song J., Zhang S. (2016) Effects of H_2S injection on the CO_2-brine-sandstone interaction under 21 MPa and 70 °C, *Mar. Pollut. Bull.* **106**, 1, 17–24.

Li Q., Li X., Niu Z., Kuang D., Ma J., Liu X., Sun Y., Li X. (2017) Effects of acid gas reinjection on enhanced natural gas recovery and carbon dioxide geological storage: Investigation of the right bank of the amu darya river, In: Y. Wu, J.J. Carroll, W. Zhu (eds), *Carbon dioxide capture and acid gas injection*. Advances in natural gas engineering, Wiley, New York, pp. 221–244. doi: 10.1002/9781118938706.ch12.

Li Q., Liu X., Du L., Bai B., Fang Z., Jing M., Li X. (2013) Economics of acid gas reinjection with comparison to sulfur recovery in China, *Energy Procedia* **37**, 2505–2510.

Liang S., Deng Y., Zhou W. (2016) Optimization selection of injecting N_2 volume in single well of Tahe fractured vuggy reservoir, *Drill. Prod. Technol.* **39**, 4, 60–62.

Liu B., Xu J., Li Z., Malekian R., Xu Z. (2018) Modeling of CO_2 transport and pressure buildup in reservoirs during CO_2 storage in saline aquifers: A case in Dongying Depression in China, *Environ. Earth Sci.* **77**, 5, 158.

Liu X., Li Q., Du L., Li X. (2012) Economic comparison of both acid-gas reinjection and sulfur recovery in high-sour gasfields, *Natural Gas Technol. Econ.* **6**, 4, 55–59.

Marini L. (2006) *Geological sequestration of carbon dioxide: Thermodynamics, kinetics, and reaction path modeling*, Elsevier.

Meng Q., Jiang X., Li D., Xie Q. (2015) Numerical simulations of pressure buildup and salt precipitation during carbon dioxide storage in saline aquifers, *Comput. Fluids* **121**, 92–101.

Miwa M., Shiozawa Y., Saito Y., Tarmoom I.O. (2002) Sour gas injection project, in: *Abu Dhabi International Petroleum Exhibition and Conference*, Society of Petroleum Engineers, Abu Dhabi, United Arab Emirates, p. 11.

Palandri J.L., Kharaka Y.K. (2004) *A compilation of rate parameters of water-mineral interaction kinetics for application to geochemical modeling*, Geological Survey Menlo Park, CA.

Pruess K., Battistelli A. (2002) *TMVOC, a numerical simulator for three-phase non-isothermal flows of multicomponent hydrocarbon mixtures in saturated-unsaturated heterogeneous media*, Earth Sciences Division, Lawrence Berkeley National Laboratory.

Pruess K., García J. (2002) Multiphase flow dynamics during CO_2 disposal into saline aquifers, *Environmental Geology* **42**, 2, 282–295.

Pruess K., Müller N. (2009) Formation dry-out from CO_2 injection into saline aquifers: 1. Effects of solids precipitation and their mitigation, *Water Resour. Res.* **45**, 3.

Reagan M. (2006) *WebGasEOS 1.0 user guide*, Earth Sciences Division, Lawrence Berkeley National Laboratory.

Schaef H.T., McGrail B.P., Owen A.T. (2010) Carbonate mineralization of volcanic province basalts, *Int. J. Greenhouse Gas Control* **4**, 2, 249–261.

Schaef H.T., Mcgrail B.P., Owen A.T., Arey B.W. (2013) Mineralization of basalts in the CO_2–H_2O–H_2S system, *Int. J. Greenhouse Gas Control* **16**, 4, 187–196.

Shen A., Zheng J., Chen Y., Ni X., Huang L. (2016) Characteristics, origin and distribution of dolomite reservoirs in Lower-Middle Cambrian, Tarim basin, NW China, *Pet. Explor. Dev.* **43**, 3, 375–385.

Talman S. (2015) Subsurface geochemical fate and effects of impurities contained in a CO_2 stream injected into a deep saline aquifer: What is known, *Int. J. Greenhouse Gas Control* **40**, 267–291.

Xiao Y., Xu T., Pruess K. (2009) The effects of gas-fluid-rock interactions on CO_2 injection and storage: Insights from reactive transport modeling, *Energy Procedia* **1**, 1, 1783–1790.

Xu T., Apps J.A., Pruess K., Yamamoto H. (2007) Numerical modeling of injection and mineral trapping of CO_2 with H_2S and SO_2 in a sandstone formation, *Chem. Geol.* **242**, 3, 319–346.

Xu T., Spycher N., Sonnenthal E., Zheng L., Pruess K. (2012) *Toughreact user's guide: A simulation program for non-isothermal multiphase reactive geochemical transport in variably saturated geologic media, version 2.0*, Earth Sciences Division, Lawrence Berkeley National Laboratory, University of California, Berkeley, CA, p. 94720.

Yu Q., Wen Z., Tang Y. (2011) Geochemical characteristics of Ordovician crude oils in the northwest of the Tahe oil field, Tarim basin, *Chin. J. Geochem.* **30**, 1, 93–98.

Zhang W., Xu T., Li Y. (2011) Modeling of fate and transport of coinjection of H_2S with CO_2 in deep saline formations, *J. Geophys. Res. Solid Earth* **116**, B02202.

Zhao R., Cheng J. (2017) Effects of temperature on salt precipitation due to formation dry-out during CO_2 injection in saline aquifers, *Greenhouse Gases Sci. Technol.* **7**, 4, 624–636.

Zheng L., Spycher N., Birkholzer J., Xu T., Apps J., Kharaka Y. (2013) On modeling the potential impacts of CO_2 sequestration on shallow groundwater: Transport of organics and co-injected H_2S by supercritical CO_2 to shallow aquifers, *Int. J. Greenhouse Gas Control* **14**, 113–127.

Zheng L., Spycher N., Xu T., Apps J., Kharaka Y., Birkholzer J. T. (2010) *Modeling studies on the transport of Benzene and H_2S in CO_2-water systems*, Office of Scientific & Technical Information Technical Reports.

Zhou Q., Birkholzer J.T., Mehnert E., Lin Y.-F., Zhang K. (2010) Modeling basin- and plume-scale processes of CO_2 storage for full-scale deployment, *Groundwater* **48**, 4, 494–514.

Zhu J., Parris T.M., Richard Bowersox J., Harris D.C. (2013) Modeling CO_2–brine–rock interactions in the knox group: Implications of a deep carbon storage field test in western Kentucky, *Appl. Geochem.* **37**, 29–42.

Ziabakhsh-Ganji Z., Kooi H. (2012) An equation of state for thermodynamic equilibrium of gas mixtures and brines to allow simulation of the effects of impurities in subsurface CO_2 storage, *Int. J. Greenhouse Gas Control* **11**, S21–S34.